PHYSICAL REVIEW B **84**, 064104 (2011)

Modeling structural transformations in binary alloys with phase field crystals

Michael Greenwood,[1,2] Nana Ofori-Opoku,[2] Jörg Rottler,[1] and Nikolas Provatas[2]
[1]*Department of Physics and Astronomy, University of British Columbia, 6224 Agricultural Road, Vancouver, British Columbia, V6T 1Z1, Canada*
[2]*Department of Materials Science and Engineering, McMaster University, 1280 Main Street West, Hamilton, Ontario, L8S 4L7, Canada*

(Received 4 July 2011; published 18 August 2011)

We develop a phase field crystal model for structural transformations in two-component alloys. In particular, the interactions between components are described by direct correlation functions that are an extension of those introduced by Greenwood *et al.* [Phys. Rev. Lett. **105**, 045702 (2010)] for pure materials. These correlation functions result in broad density modulations that can be treated with high numerical efficiency, hence enabling simulations of phase transformations between a wide range of crystal structures. A simplified binary alloy model is shown to describe the equilibrium properties of eutectic and peritectic binary alloys in two and three dimensions. The robustness and versatility of this method is demonstrated by applying the model to the growth of structurally similar and dissimilar eutectic lamella and to segregation to defects.

DOI: 10.1103/PhysRevB.84.064104 PACS number(s): 64.70.K−, 61.50.Ah, 81.10.Aj, 46.15.−x

I. INTRODUCTION

The properties of engineering alloys are intimately connected to the patterning of their internal microstructure, which is established during solidification and thermomechanical processing. Many fundamental processes controlling phase selection and microstructure morphology are understood largely via empirical methods. This is partly because *in situ* measurements of phenomena such as nucleation, dislocation-interface, and dislocation-solute interactions, etc., are extremely difficult, if not impossible to perform. Moreover, many of the basic theoretical mechanisms at work during nonequilibrium phase transformations, which ultimately guide the development of microstructure, are poorly understood.

Progress in predicting microstructure formation during materials processing has seen great advances in recent years, particularly through the use of modeling techniques capable of integrating mass and heat transport with the kinetics of interface evolution. One such technique is the phase field model, which has as its heart the dissipative minimization of a free-energy functional that is expressed in terms of spatially varying fields that describe impurities, temperature, and the phases that evolve and interact during phase transformations. Early works involving phase field models helped shape the prevailing understanding about the role of process and material parameters on the kinetics of crystallizing structures.[1–9] More recent phase field studies have incorporated additional physical mechanisms such as strain relaxation through coupling to solute-lattice interactions, dislocations, external strains, and lattice misfits. Such models have afforded valuable understanding of topics that range from the role of strain on dislocation flow[10,11] to the effect of elastic anisotropy on preferred precipitate growth directions.[12–14]

A longstanding weakness of traditional phase field models has been their formulation in terms of spatially uniform fields and the use of effective parameters. The latter issue — a vestige from their emergence from mean-field theory—requires that phase field models be asymptotically mapped onto their sharp interface limit in order to be made quantitative. The former issue precludes the self-consistent incorporation of elastic and plastic phenomena that inherently arise from atomically periodic states. These include elastic strain, dislocations, structured grain boundaries and structural transformations.

An exciting extension to the phase field paradigm, coined the phase field crystal (PFC) method, has recently been advanced by using free-energy functionals that are minimized by periodic, rather than uniform, order parameters. This began with the work of Elder *et al.*,[15,16] who modeled crystallization using a free-energy functional that is minimized by triangular structures in two dimensions and bcc structures in three dimensions. This description was shown to capture the salient physics of grain boundaries, misfit strains, dislocation climb, and glide in metallic systems. A modification to the basic PFC dynamics was developed to describe a host of phenomena governed by rapid strain relaxation.[17] Elder and co-workers later extended the formalism to binary alloys.[18] When the PFC order parameter is interpreted as an atomic number density, the same work (as well as Jin and Khachaturyan[19]) showed that it is formally possible to derive all phenomenological phase field crystal variants from the more microscopic classical density functional theory (CDFT).

Despite the tremendous success of the initial PFC models, two crucial features have been conspicuously missing from the formalism. The first is the ability to generate a robust range of stable crystal structures. The second is the ability to model realistic material phase diagrams. Recently, Greenwood *et al.*[20,21] introduced a PFC formalism that begins with the free-energy functional of CDFT. The ideal (entropic) contribution of the free energy is expanded around the reference state to quartic order, and interactions are encoded in a two-point direct correlation function in reciprocal space that possesses peaks for each family of lattice planes present in a desired crystal structure. The relative heights of each family's peaks are modulated by a Debye-Waller–like exponential decay through a phenomenological temperature parameter. Retaining only the lowest order peaks of each planar family in the (directionally averaged) correlation function allows for a minimal energy kernel which produces broad "real space" density peaks—a

©2011 American Physical Society

crucial feature if the method is to stand any chance of being numerically efficient. The modulation of the relative peak heights makes it possible to simulate two-dimensional (2D) square and triangular lattices and three-dimensional (3D) fcc, bcc, hcp, and simple cubic (sc) lattices. More importantly, it allows for different variants of these phases to coexist with each other and with a liquid phase. Finally, by introducing a tunable width for each peak, this approach makes it possible to separately adjust the elastic coefficients of different phases.

This paper extends the approach developed by Greenwood *et al.* to the case of two-component alloys. We begin with the CDFT free-energy functional for two-component A and B mixtures. We model A-A and B-B interactions using the single-component correlation function introduced in Refs. 20 and 21. Interactions between A and B atoms are modeled by interpolating single-component correlations as a function of the local concentration of impurities. We showcase the equilibrium properties of our formalism by computing several alloy phase diagrams. We then demonstrate the robustness of our method by simulating eutectic phases with differing crystal symmetries. Finally, we illustrate the applicability of our model to solute segregation and elastic anisotropy.

II. FREE-ENERGY FUNCTIONALS FOR BINARY ALLOYS

The free energy for a binary PFC model can be written as a combination of the energy of the two density fields separately and a component including their interaction. As with the pure model, these components are broken into two types. The first component is a purely entropic local energy density ΔF_{id} responsible for driving the density to uniform fields (i.e., disordered phases such as a liquid). The second component is an excess free-energy density ΔF_{ex} which drives the density fields to form periodic structures (i.e., crystals). The excess energy is responsible for elasticity in crystalline phases, as well as for the interaction of topological defects such as dislocations and interfaces. The total free energy is written in dimensionless form as

$$\frac{\Delta F}{kT\rho^o} = \int \left(\frac{\Delta F_{id}}{kT\rho^o} + \frac{\Delta F_{ex}}{kT\rho^o} \right) d^3r, \tag{1}$$

where ρ^o is a reference state density, k the Boltzmann constant, and T the temperature.

The purely entropic component of the free energy contains the sum of the ideal free energy of the individual fields ρ_A and ρ_B,

$$\frac{\Delta F_{id}}{kT} = \rho_A \ln\left(\rho_A/\rho_A^o\right) - \delta\rho_A + \rho_B \ln\left(\rho_B/\rho_B^o\right) - \delta\rho_B. \tag{2}$$

Following Elder *et al.*,[18] we define the total mass density per unit volume as $\rho = \rho_A + \rho_B$ and write the total reference density of the system as the sum of the two independent reference states of A and B, $\rho^o = \rho_A^o + \rho_B^o$. As in Provatas *et al.*,[22] we also define an atomic number fraction of B atoms, i.e., solute concentration, as $c = \rho_B/(\rho_A + \rho_B)$ and a corresponding reference composition $c_o = \rho_B^o/\rho^o$. For convenience, we further define a dimensionless density field via the definition $n = \rho/\rho^o - 1$. In terms of the concentration c and the dimensionless density n, the ideal free-energy density can be recast as

$$\frac{\Delta F_{id}}{kT\rho^o} = (n+1)\ln(n+1) - n + (n+1)\left[c \ln\left(\frac{c}{c_o}\right) + (1-c)\ln\left(\frac{1-c}{1-c_o}\right)\right]. \tag{3}$$

The excess free-energy density is expanded to second order in the density, using two-point correlation functions to describe A-A, B-B, or A-B interactions, namely,

$$\Delta F_{ex} = \sum_{ij} \Delta F_{ij} = -\frac{1}{2}\sum_{ij} \delta\rho_i(r) \int dr' C_2^{ij}(|r-r'|)\delta\rho_j(r'), \tag{4}$$

where C_2^{ij} describes the correlation of species i with the field-describing species j. This expression can alternatively be written in terms of the dimensionless density field n and the composition field c. To proceed, we make the assumption that the solute concentration c varies on much larger length scales than the periodicity of the density field n. It is important to appreciate that the PFC model does not localize individual vacancies and solute atoms but allows them to relax rapidly on diffusive time scales. This implies that we can make the approximation $c(r') \to c(r)$ in the integrals appearing in Eq. (4). For example,

$$\int dr' C_2^{ij}(|r-r'|)n(r')c(r') \approx c(r)\int dr' C_2^{ij}(|r-r'|)n(r'). \tag{5}$$

To simplify notation, hereafter we use the the notation that $n(r') = n'$ and $c(r') = c'$. Furthermore, in what follows it will be assumed that the $k = 0$ mode of all correlation functions is zero. As discussed for the case of a pure material in Greenwood *et al.*,[21] a nonzero amplitude peak at $k = 0$ in the correlation function shifts the free energies when the mean density *deviates* from the reference state, thus changing the phase diagram in the density dimension; for the bulk phases at the reference density the $k = 0$ mode has no contribution to the free energy. With these assumptions, we arrive at the following excess free-energy density

$$\begin{aligned}\frac{\Delta F}{kT\rho_o} = \int dr \frac{n^2}{2} - \eta\frac{n^3}{6} + \chi\frac{n^4}{12} + (n+1)\Delta F_{\text{mix}}(c) \\ -\frac{1}{2}n\left(\int dr' C_{\text{eff}}^{n} n' + \int dr' C_{\text{eff}}^{c} c'\right) \\ -\frac{1}{2}(c-c_o)\left(\int dr' C_{\text{eff}}^{c_o n} n' + \int dr' C_{\text{eff}}^{c_o c} c'\right),\end{aligned} \tag{6}$$

where the prefactors η and χ are added as fitting parameters to fit the ideal energy to a polynomial expansion ($\eta = \chi = 1$ corresponds to a Taylor series expanded around the reference density) and $\Delta F_{\text{mix}}(c)$ denotes the entropy of mixing,

$$\Delta F_{\text{mix}}(c) = \left\{c \ln\left(\frac{c}{c_o}\right) + (1-c)\ln\left(\frac{1-c}{1-c_o}\right)\right\}. \tag{7}$$

The effective correlation functions in the excess free energy are modulated by the composition as

$$\begin{aligned}C_{\text{eff}}^{n} &= c^2 C_2^{BB} + (1-c)^2 C_2^{AA} + c(1-c)\left(C_2^{BA} + C_2^{AB}\right),\\ C_{\text{eff}}^{c} &= c\left(C_2^{BB} - C_2^{BA}\right) - (1-c)\left(C_2^{AA} - C_2^{AB}\right),\end{aligned}$$

$$C_{\text{eff}}^{c_o n} = c\big(C_2^{BB} - C_2^{AB}\big) - (1-c)\big(C_2^{AA} - C_2^{BA}\big),$$
$$C_{\text{eff}}^{c_o c} = C_2^{BB} + C_2^{AA} - \big(C_2^{BA} + C_2^{AB}\big). \tag{8}$$

A. Simplified binary free-energy functional

The model in Eq. (6) can be further simplified by coarse graining the various terms. Following, for example, the coarse-graining procedures in Refs. 22–25, it is straightforward to show that the cross terms in n and c vanish in the long-wavelength limit, since the density oscillates rapidly about $n = 0$ and c is a smooth field. Meanwhile, the second-order correlation term in c gives, to leading order, a gradient term in c, analogous to those in Cahn-Hilliard theory. The technical details of coarse graining the various terms in the free energy are not reproduced here.

The assumptions of the previous paragraph lead to the following simplified dimensionless alloy PFC free-energy functional

$$\frac{\Delta F}{kT\rho_o} = \int dr \left\{ \frac{n^2}{2} - \eta\frac{n^3}{6} + \chi\frac{n^4}{12} + (n+1)\Delta F_{\text{mix}}(c) - \frac{1}{2}n\int dr' C_{\text{eff}}^{n}(|r-r'|)n' + \alpha|\vec{\nabla}c|^2 \right\}. \tag{9}$$

The entropy of mixing $\Delta F_{\text{mix}}(c)$ is modified according to

$$\Delta F_{\text{mix}}(c) \rightarrow \omega\left\{ c\ln\left(\frac{c}{c_o}\right) + (1-c)\ln\left(\frac{1-c}{1-c_o}\right)\right\}. \tag{10}$$

The parameter α is introduced to subsume any dependency on $C_{\text{eff}}^{c_o c}$ of the square gradient term in c, which emerges from coarse graining Eq. (6).

Equation (9) has the form of a Cahn-Hilliard model [when $\Delta F_{\text{mix}}(c)$ is expanded] plus a PFC contribution for the total density analogous to that in Greenwood *et al.*[21] Furthermore, the parameters η, χ, and ω are introduced to fit the ideal energy away from the reference density ρ_o and entropic energy away from the reference composition c_o. This can be motivated by noting that higher-order correlation functions would yield corrections to the density expansion, as recently shown by Huang *et al.*[25] For convenience, ΔF_{mix} is left as in Eq. (10), rather than expanding in powers of c.

B. Correlation functions

The effective correlation function $C_{\text{eff}}^{n}(|r-r'|)$ in the free energy is a polynomial interpolation of C_2^{AA}, C_2^{BB}, C_2^{AB}, and C_2^{BA}, weighted by the composition field. The correlation functions C_2^{AB} and C_2^{BA} represent, respectively, contributions to the excess free energy for the cases where A atoms are in a crystalline structure preferred by B atoms and B atoms that are in a structure preferred by A atoms. In this respect we can approximate these correlation functions by a composition-modulated interpolation between C_2^{AA} and C_2^{BB}. We thus introduce here a form for C_{eff}^{n} given by

$$C_{\text{eff}}^{n} = X_1(c)C_2^{AA} + X_2(c)C_2^{BB}, \tag{11}$$

where

$$X_1(c) = 1 - 3c^2 + 2c^3$$
$$X_2(c) = 1 - 3(1-c)^2 + 2(1-c)^3 \tag{12}$$

are interpolation functions which interpolate between the two correlation functions, weighting each as a function of the local composition, analogous to finite-element shape functions.

Each alloy component has as input to the model its own correlation function, thus influencing the preferred structure for that component and free energy changes due to local structural changes. The correlation functions $C_2^{ii}(|\vec{k}|)$ are constructed to include relevant reciprocal space peaks at positions determined by each component's equilibrium crystal unit cell structure. The positions of the peaks correspond to the crystallographic Bragg peaks for a particular element's structure. The curvature at the tips of each Bragg peak is tuned to fit the elastic coefficients, while the heights of the peaks are linked to the temperature. The method for this construction is described in detail in Ref. 21. These effects are all crucial in driving structural transformations.

C. Model dynamics

The dynamics of the total density and concentration fields obey the usual dissipative dynamics applied to each species density (i.e., ρ_A and ρ_B). Following the procedure in Elder *et al.*,[18] this translates to the following equations of motion for n and c:

$$\frac{\partial n}{\partial t} = \vec{\nabla}\cdot\left\{ M_n(\vec{r})\vec{\nabla}\left[n - \eta\frac{n^2}{2} + \chi\frac{n^3}{3} + \Delta F_{\text{mix}} - \int C_{\text{eff}}^{n} n' \right]\right\}, \tag{13}$$

$$\frac{\partial c}{\partial t} = \vec{\nabla}\cdot\left\{ M_c(\vec{r})\vec{\nabla}\left[(n+1)\frac{\delta\Delta F_{\text{mix}}}{\delta c} - \alpha\nabla^2 c - \frac{1}{2}n\int\frac{\delta C_{\text{eff}}^{n}}{\delta c}n' \right]\right\}. \tag{14}$$

Note that these equations are fully deterministic; conserved noise may be added to the fields to facilitate nucleation and transitions over barriers[25] but is not used in this paper.

III. EQUILIBRIUM PROPERTIES OF THE MODEL

This section examines the equilibrium properties of the simplified binary alloy PFC model presented above. First we outline the method of phase-diagram construction and how each component in the free-energy functional affects the shape of the phase coexistence lines. We then consider several case studies. First we look at the case where A and B solids are both structurally similar by examining a phase diagram for a 2D square-square transition. Second we examine in two dimensions a eutectic transformation between two structurally different components for the case of square and triangular solid phases. Finally, we consider 3D bcc and fcc structures that form a peritectic phase diagram.

A. Phase-diagram construction method

The phase coexistence between the respective phases is determined by a common tangent construction between the free-energy curves of the bulk phases at the reference density ($\bar{n} = 0$). We calculate the energy curves by considering single-mode approximations for the bcc and triangular phases and two-mode approximations for the fcc and square phases. It was shown in Ref. 21 that the energy contribution due to additional modes for the bcc and triangular phases in the PFC approximation is small and is thus neglected. The periodic phases (square, triangle, fcc, and bcc) are approximated by the sum of these density modes as defined by

$$n_i(\vec{r}) = \sum_j A_j \sum_l e^{2\pi \mathbf{i} \vec{k}_l \cdot \vec{r}/a_i}, \tag{15}$$

where the subscript i denotes a particular solid phase, i.e., $i = \text{fcc}$ represents an fcc ordering with lattice spacing a_{fcc}, j is the index over the included modes of the i phase, A_j is the amplitude of mode j, and l is the index over the collection of reciprocal space peaks corresponding to mode j. Accordingly, $\vec{k}_l$ is the reciprocal lattice vector normalized to a lattice spacing of 1, corresponding to each index l.

The correlation functions for each pure phase, C_2^{AA} and C_2^{BB}, are constructed like those in Refs. 20 and 21. Specifically, a reciprocal space peak of C_2^{ii} corresponding to mode j has the general form

$$\hat{C}^{ii}_{2j} = e^{-\frac{\sigma^2 k_j^2}{2\rho_j \beta_j}} e^{-\frac{(k-k_j)^2}{2\alpha_j^2}}, \tag{16}$$

where $ii = \text{AA, BB}$. The total kernel $\hat{C}_2^{ii}$ is taken as the envelope of all peaks $\hat{C}^{ii}_{2j}$ included to represent the atomic interactions. When the peaks do not overlap, $\hat{C}_2^{ii}$ can be treated as the simple sum of all peaks. This construction defines the peak positions and widths in the correlation kernel from each family of planes in a given unit cell. The first exponential term in Eq. (16) includes the effect of temperature through a Debye-Waller–like amplitude modulation, with σ playing the role of an effective temperature, ρ_j the atomic density of the plane, and β_j being the planar symmetry. The second exponential sets the peak positions of the reciprocal lattice vector k_j and is of Gaussian form with width α_j. By varying α_j we can take into account surface energy, defects, and elastic properties.

An equilibrium phase diagram can be constructed via the simplified binary free energy in Eq. (9) as follows. Energy curves as a function of the composition c are calculated by inputting the density field approximation of Eq. (15) for each structural phase into Eq. (9) and integrating over the unit cell. The resulting free energy is then minimized with respect to the amplitudes A_j. The liquid-phase free energy is found by setting $A_j = 0$ and the density to the reference density (i.e., $\bar{n} = 0$). A common tangent construction is then performed on the resulting solid and liquid phases. This methodology is outlined in more detail in the Appendix. Some binary phase diagrams relevant to materials science phenomena are examined below.

B. Eutectic alloys

First we demonstrate the equilibrium properties of an alloy where the elements are structurally similar, only differing in the equilibrium lattice spacings of their constituent elements. Each element is represented by a correlation function C_2^{ii}, where the structure produced for each element is topologically identical, i.e., the number of peaks and the ratio of their positions in Fourier space is identical. However, they differ in the absolute position of the peaks and through the width of each peak through α_j, thus producing different equilibrium lattice spacings, elastic, and surface energies for each element. Giving both elements square symmetry leads to the phase diagram shown in Fig. 1, while the inset shows the corresponding phase diagram for a triangle-triangle binary system. Both diagrams are asymmetric with clearly defined eutectic points and metastable coexistence lines (gray dotted). In the solid solution phases Sq$_A$ and Sq$_B$ the density field n will take the structure corresponding to the effective correlation function, while the concentration field is relatively uniform with small amplitude modulations that follow the density field.

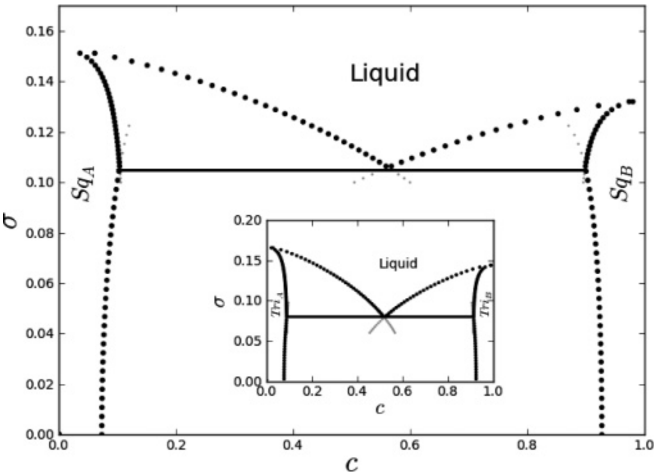

FIG. 1. Phase diagram for a square-square system with the inset showing the phase diagram of a triangle-triangle mixture. The equilibrium coexistence lines are shown in thick black dots and metastability lines are shown in thin gray dots. The phase diagrams share identical parameters for the noninteracting parts of the energy. Specifically, the parameters for the ideal free-energy contribution were $\eta = 1.4$, $\chi = 1$, while $\omega = 0.02$ and $c_0 = 0.5$ for the entropy of mixing. For the square-square system, the widths of the correlation peaks (i.e., the setting of the elastic coefficients) correspond to $\alpha_{11A} = 0.9$, $\alpha_{10A} = \sqrt{2}\alpha_{11A}$, $\alpha_{11B} = 0.9$, and $\alpha_{10B} = \sqrt{2}\alpha_{11B}$. The peak positions for species A correspond to $k_{11A} = 2\pi$ and $k_{10A} = \sqrt{2}k_{11A}$ and for species B, $k_{11B} = 4\pi/\sqrt{3}$ and $k_{10B} = \sqrt{2}k_{11B}$. For the triangle-triangle system, peak widths are $\alpha_{10A} = 0.8$ and $\alpha_{10B} = 0.8$ and peak positions are $k_{10A} = 2\pi$ and $k_{10B} = 4\pi/\sqrt{3}$.

Phase diagrams can also be constructed for structurally dissimilar elements. Here we choose element A to have a correlation function with square symmetry by including two peaks in C_2^{AA}, while element B has a correlation function corresponding to a triangular structure and therefore only contains a single peak in C_2^{BB}. In this case we make the atomic diameter dimensionally 1 for both the square and triangle lattices. Using the method described above gives the eutectic phase diagram in Fig. 2(a).

Using the conserved dissipative dynamics described by Eqs. (13) and (14) we can test the validity of the approximations made in our phase-diagram construction. Square and triangular phases of the equilibrium lattice spacing are initially seeded in a narrow channel at a composition close to the equilibrium composition, as predicted by the phase diagram for a small seed. The liquid phase, represented by a constant density field, is set to a composition such that the

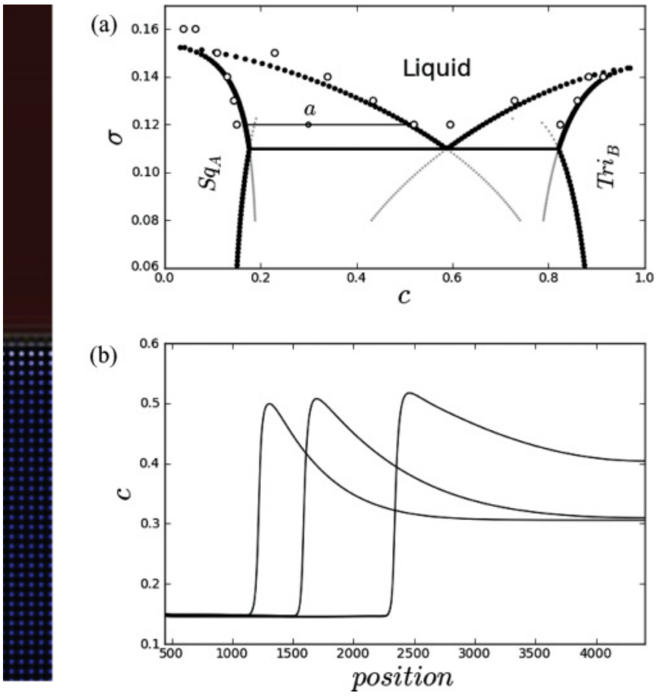

FIG. 2. (Color online) Eutectic system for two structurally dissimilar elements. (a) Phase diagram for a mixture of element A (square) and element B (triangle); solid dots are equilibrium points calculated via the single-mode expansion method described in the text, gray dots depict metastable coexistence points, and open circles are dynamic simulations. The parameters for the ideal energy are $\eta = 1.4$, $\chi = 1$, while $\omega = 0.02$ and $c_0 = 0.5$ for the entropy of mixing. For the square structure, the widths of peaks and peak positions are $\alpha_{11A} = 1.5$, $\alpha_{10A} = \sqrt{2}\alpha_{11A}$ and $k_{11A} = 2\pi$, $k_{10A} = \sqrt{2}k_{11A}$. The triangular structure has peak width and position corresponding to $\alpha_{11B} = 1.5$ and $k_{11B} = 4\pi/\sqrt{3}$. (b) Time slices of an evolving compositional profile through a solid-liquid interface corresponding to a quench to point "a" in the phase diagram. A corresponding density-concentration profile of the advancing 1D solid-liquid interface in a channel is shown on the left. The color represents local composition, where blue is saturated at $c = 0.1$ and red is $c = 0.6$.

mean system composition has a value in the coexistence region of the phase diagram. An example of such a setup is depicted in Fig. 2 (left). The composition between the solid and liquid phases naturally segregates during the growth of the front, producing a lengthening diffusion tail ahead of the interface until the interface eventually comes to rest, as expected in one-dimensional (1D) diffusion-limited front growth. A sequence of evolving compositional profiles is shown in Fig. 2(b). After obtaining equilibrated composition profiles such as these over several temperatures in both the square-liquid and triangle-liquid coexistence regions, we compare the resulting bulk concentrations to the analytic phase diagram in Fig. 2(a). We find that removing the temperature dependence of the ratio of the two amplitudes (A_{11}:A_{10}) corresponding to the two square correlation peaks (i.e., use the ratio at $\sigma = 0$ for all temperatures) results in good agreement at low temperatures, but it begins to deviate as the temperature increases. This approximation is detailed in the Appendix.

Eutectic systems modeled by our PFC alloy formalism exhibit all the essential features required to investigate elastic and plastic phenomena in phase transformations in experimentally relevant alloy systems. One such phenomenon involves eutectic growth under different processing conditions and in which the constituent lamellae may assume different crystal symmetries. Another scenario occurs when the lamellae have the same crystal structure but are lattice mismatched at their common interface. Example simulations of these situations are shown below.

C. Peritectic alloys

The model is easily extended to three dimensions, where it can describe bcc-fcc transformations. We present here a particular construction of a phase diagram for structural transformations that features a peritectic point akin to the Fe-Ni phase diagram. The resulting phase diagram is shown in Fig. 3(a), while a simpler isomorphous fcc liquid-phase diagram is shown in Fig. 3(b). These two classes of phase diagrams can be obtained by controlling the underlying lattice spacing, preferred crystal structure, and relative phase transformation temperature of each species.

For the Fe-Ni–type phase diagram in Fig. 3(a), we consider two elements of similar atomic radii: element A, with a normalized diameter of 1, and element B, with a normalized diameter of 1.016. Element A transforms at high temperature (σ) from the liquid phase into the bcc phase. At a lower temperature element A has a more energetically stable phase, the fcc symmetry. Element B transforms directly from the liquid phase into the fcc symmetry at a temperature between that of element A's transformation point from liquid to bcc and bcc to fcc. Both elements have a stable fcc phase at sufficiently low temperatures.

As discussed in Ref. 21, a bcc symmetry emerges when free-energy kernels are dominated by a single peak while fcc phases become increasingly stable for kernels that have two modes of comparable strength, the second of which corresponds to the second dominant Bragg peak of the reciprocal lattice. For both element A and B we use a kernel comprised of two peaks corresponding to an fcc symmetry. For element A to undergo a transformation from liquid to bcc to fcc, the second peak of its correlation kernel must be comparable to the first peak at low temperatures and negligible as its σ approaches the melting temperature (i.e., leaving a one-peak kernel). On the other hand, element B must maintain the relative heights of the two peaks over the entire range of the stable fcc phase.

The mechanism to engineer the properties of the correlation function described in the previous paragraph is already buried within the Debye-Waller decay of each peak. To make this more clear, the Debye-Waller prefactor to the correlation function peaks can be redefined by introducing an effective transition temperature $\sigma_{Mj}^2 = (2\beta_j\rho_j)/k_j^2$ in Eq. (16) such that each peak is now defined as

$$\hat{C}_{2j}^{ii} = e^{-\frac{\sigma^2}{\sigma_{Mj}^2}} e^{-\frac{(k-k_j)^2}{2\alpha_j^2}}. \tag{17}$$

Each peak now has its own scaling factor, allowing the transition temperature from a liquid to a bcc or from a liquid to an fcc phase to be controlled independently. Thus, for element

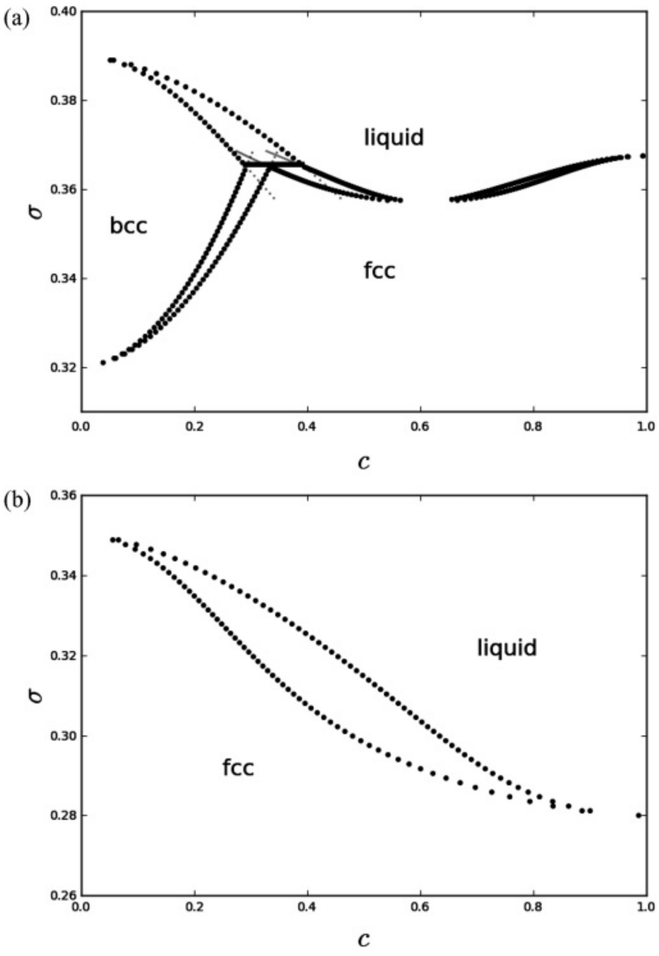

FIG. 3. Phase diagram for 3D fcc-bcc mixtures. In both cases the ideal and mixing terms of the free energy are set to $\eta = 1.3$, $\chi = 1$, and $\omega = 0.01$, and a reference composition of $c_o = 0.5$. Thick black dots and thin gray dots represent the equilibrium and metastable coexistence lines, respectively. (a) Peritectic phase diagram. The widths of the correlation peaks are set to $\alpha_{111A} = 0.4$, $\alpha_{100A} = 0.4$, $\alpha_{111B} = 0.6$, and $\alpha_{100B} = 0.6$, and the effective transition temperatures are set to $\sigma_{M111A} = 1.2$, $\sigma_{M100A} = 0.8$, $\sigma_{M111B} = 1.05$, and $\sigma_{M100B} = 1.05$ for elements A and B, respectively. (b) Isomorphous phase diagram for two elements transforming from liquid to fcc symmetries. The widths of the correlation peaks are set to $\alpha_{111A} = 0.8$, $\alpha_{100A} = 0.8$, $\alpha_{111B} = 0.9$, and $\alpha_{100B} = 0.9$ and the effective transition temperatures are set to $\sigma_{M111A} = 1.0$, $\sigma_{M100A} = 1.0$, $\sigma_{M111B} = 0.8$, and $\sigma_{M100B} = 0.8$, for elements A and B, respectively.

A we require a transition at high temperature to the bcc phase and at a lower temperature from the bcc phase to the fcc phase. Setting the σ_{Mj} parameter corresponding to the first peak to be larger than that of the second peak causes a transition from a single-peak-dominated kernel to a two-peak-dominated kernel in the region of stability over the liquid phase, i.e., bcc at high temperature, fcc at low temperature.

For element B we desire solidification directly to fcc. In this case at high temperature a two-peak-dominated kernel is needed, so the Debye-Waller coefficients σ_{Mj} for both peaks are set to the same value, i.e., they both raise and lower comparably with temperature (σ). This leads to solidification from liquid directly to the fcc phase, which remains stable (over the bcc structure) at all temperatures below the transition temperature. However, recall that element B was chosen to have a lower melting temperature than element A. Then σ_{M1A} for the first peak of A must be larger than σ_{M1B} for the first peak of element B. A phase diagram for this type of scenario is illustrated in Fig. 3(a).

Construction of an isomorphous phase diagram between liquid and fcc phases is also possible. For both elements A and B the liquid transforms directly to the fcc phase; however, this transformation occurs at different temperatures for both phases. Keeping the lattice spacings given above for the peritectic phase diagram, the effective transition temperatures σ_{Mj} for each element are set such that the density field transforms from liquid to fcc but at different effective temperatures at each composition. The difference between the effective temperatures and the difference in the correlation peak widths (α_j) of each element cause an asymmetry in the energy about the liquid energy, producing an isomorphous phase diagram as shown in Fig. 3(b).

The phase diagrams shown here demonstrate the robustness of our model to generate, through the parameters introduced, various types of materials phase diagrams. Several approximations were made in the calculation of the phase diagrams and their numerical validation for the case of the square-triangle system. The analytic and numerical phase boundaries were in good agreement, with minor deviations as expected, due to the limitations of the one and two mode expansions. It is noted that unlike previous binary PFC models, we opted here to keep the full form of the entropy-of-mixing term rather than expanding it in a power series. Also, we considered two different amplitudes for the case of two-mode structures. In the Appendix we demonstrate the changes that occur when a single amplitude is used for the expansion of the density of multimode structures. We find that the physics, i.e., the general type of alloy and form of the phase diagram, does not change; however, there are shifts in the phase diagram.

IV. APPLICATIONS

The PFC approach opens the door to a myriad of possible applications that require atomic-level elastic and plastic effects to properly capture the physics of anisotropy, elasticity, and defects that occur over the diffusive time scales on which phase transformations take place. This section uses some of the alloy systems derived above to demonstrate their application to two practical materials phenomena. The first is the solidification of eutectic lamella that are both structurally similar and dissimilar. The second application deals with solute segregation of composition around defects.

A. Eutectic lamellae growth

Growth mechanisms ranging from dendritic growth in solidification to grain growth in the solid state are widely studied throughout materials science. Where single dendritic growth and grain growth is concerned, there is a plethora of theoretical, experimental, and numerical works that have been put forth. Comparatively less work has been done on the subject of eutectic growth. One aspect in particular that has been lacking in previous phase field and related theoretical studies of eutectic growth is the exclusion of structural and elastoplastic effects that occur during the co-operative growth of lamellar phases. The present model, having the capability to describe phases with differing structures, elasticity, plasticity, and chemical interactions as well as defects, offers an avenue from which we can investigate eutectic growth under realistic conditions. Below we showcase qualitatively the growth of eutectic lamellae when the two elements are structurally similar but have different preferred atomic spacings.

We use the structurally similar phase diagrams for the square-square binary system calculated above and show the results in Fig. 4. All simulations were conducted in a domain of $10{,}000\Delta x \times 2000\Delta x$, which corresponds approximately to 1500×300 lattice spacings. Uniform mesh and time spacings of $\Delta x = 0.15$ and $\Delta t = 3$ were used and the dynamical equations were solved semi-implicitly in Fourier space for greater stability and efficiency. The initial condition consists of eight individual lamellae, four of each phase or structure, and each approximately 22×37 lattice spacings and with concentration corresponding to the tie line for the given temperature below the eutectic, $\sigma = 0.09$. Since our structures already have a lattice mismatch, we have only considered, for simplicity, those cases when there exists an orientational mismatch. We have taken several time slices through the evolution of lamellar colonies for each misorientation as shown in Fig. 4 for the square system. We have also examined an example for growth of lamellae with structurally dissimilar crystal structures in Fig. 5.

As the misorientation between the lamellae is altered, the coarsening rate, growth rate, and spacing of the lamella are different due to the surface energy differences and elastic interactions as well as differences in the short-circuit diffusion paths between lamella. The influence of the misorientation of the lamella is clearly shown in the late time images of Fig. 4. Different misorientations can lead to different pinch-off rates. When a particular lamella is pinched off there is a temporary depletion of the solute and the system must locally wait for solute to diffuse laterally in order to continue its growth. It is this pinching off and coarsening process that ultimately leads to the final structure. These behaviors are related to the solid-solid and solid-liquid interfacial energies and the coherency of the interface as a function of the misorientation between lamellae and the lattice mismatch. The model allows us to study the effect of the mismatched lattices, misorientations, and the effect of the elastic and surface anisotropy in a very natural way.

For the simulations presented above, there were several factors that determined suitable initial conditions from which to proceed. Aside from the general mismatch between the two structures, we also had to contend with the effects of finite size from both the simulation domain as well as the size of the lamellae. With an insufficient domain size, one is restricted to a certain size of lamellae, having no guarantee that the lamellae chosen will grow due to a finite-system size strain. If growth does occur, however, it will not be cooperative growth, such as the growth shown in the above figures. If the domain size is sufficiently large enough, then size of the lamellae should be chosen so that cooperative growth is observed. In our simulations we find that each of the lamella should not be less than approximately $20-30$ lattice spacings. It is noted that in experimental conditions, lamellae can grow in confined interdendritic spaces, making some of these above observations relevant to describe their growth.

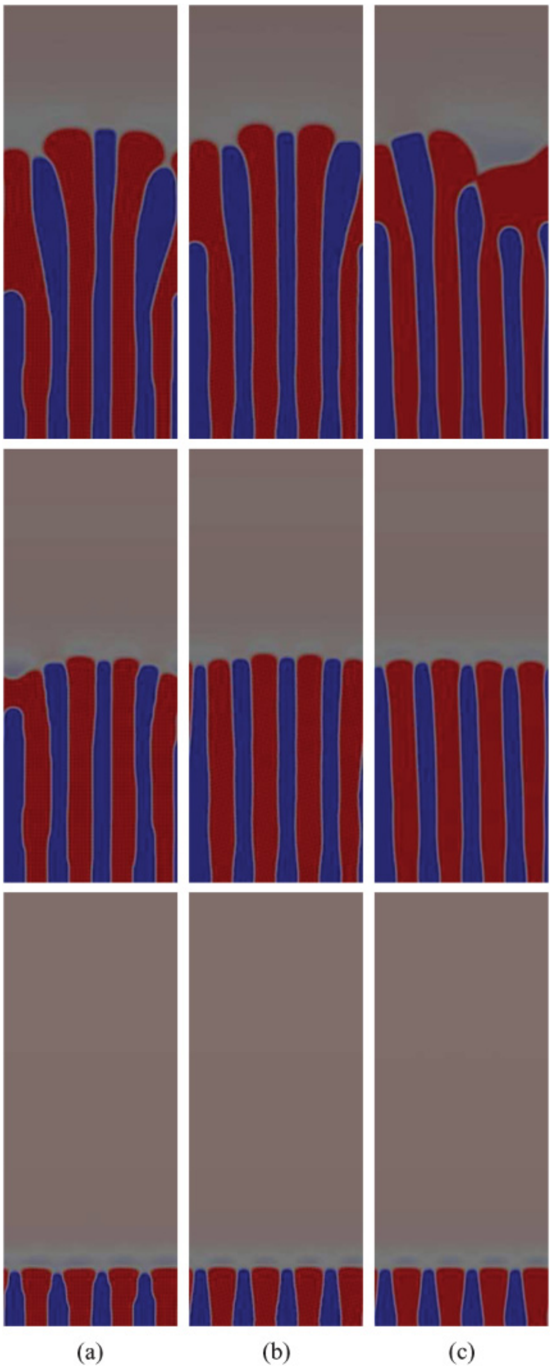

FIG. 4. (Color online) Portions of the simulation domain from the eutectic growth channels simulated with the free energy producing the square-square phase diagram of Fig. 1. The temperature is quenched to $\sigma = 0.09$ at an average concentration of $\bar{c} = 0.56$. Here the color represents concentration, with low concentration being blue (Sq_A) and high being red (Sq_B). Each column of images represents a different misorientation angle of the low-concentration lamella relative to the high-concentration lamella. The misorientations shown are (a) 0, (b) 4, and (c) 20 degrees. The simulation times are increasing from bottom to top.

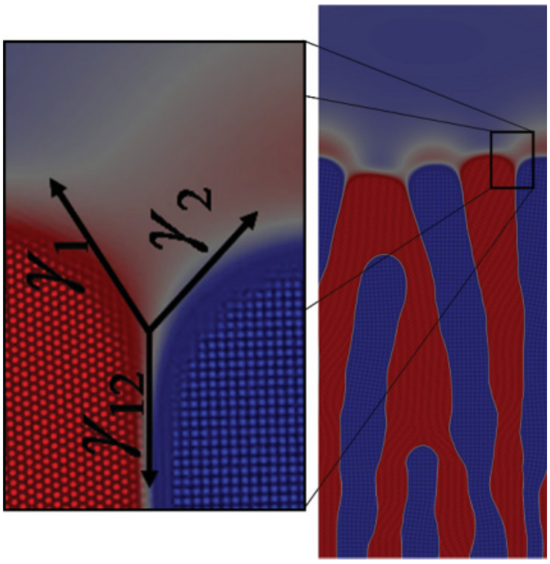

FIG. 5. (Color online) Portion of the simulation domain from the eutectic growth channel with structurally different phases. Element A prefers to solidify to a square symmetry and element B prefers to solidify to a triangular symmetry. In these structurally different lamellae the surface energy between the triangle-liquid interface (γ_1), square-liquid interface (γ_2), and the square-triangle interface (γ_{12}) are set by the correlation kernel variables α_{Ai} and α_{Bi}.

B. Compositional segregation

Segregation of solute atoms to defects and boundaries occurs due to both chemical and elastic driving forces. Our PFC model is ideally suited to study such interactions given the control of both structural and elastic properties through the correlation kernel. We consider here an example of segregation in a two-component alloy in 2D, where element A prefers a square symmetry and element B prefers a triangular structure. By alloying these two elements at B-atom concentration of $c = 0.1$, we can use the model to investigate the equilibrium segregation of solute element B to a defect at a boundary. Consider a low-angle tilt boundary made of an array of dislocations with a large interdislocation spacing where the bulk structure is dominated by element A in the square phase. The elastic parameters of pure materials A and B can be set by matching the correlation peak widths for each element. The initial composition field is set to be uniform everywhere. Using the dynamics of Eqs. (13) and (14), the system is allowed to relax in both composition and density. We consider two cases here. The first, shown in Fig. 6(a), is an elastically isotropic square phase with a solute element B preferring the triangle phase. The second case, shown in Fig. 6(b), is an elastically anisotropic square phase with a solute element B preferring the triangle phase.

There are three effects of the choice of relative elastic coefficients between elements A and B displayed here. For the first effect, we note that the bulk modulus of the square phase is proportional to the inverse sum of the widths of these two peaks, i.e., $C_{11} + C_{12} \propto \alpha^{-2}$ (Ref. 21). Thus the elastic stiffness is changed by increasing or decreasing the two peak widths. As illustrated by Fig. 6, the amount of solute that segregates to the defect is smaller when the matrix element is more pliable (a) and increases when the matrix element is stiffer (b).

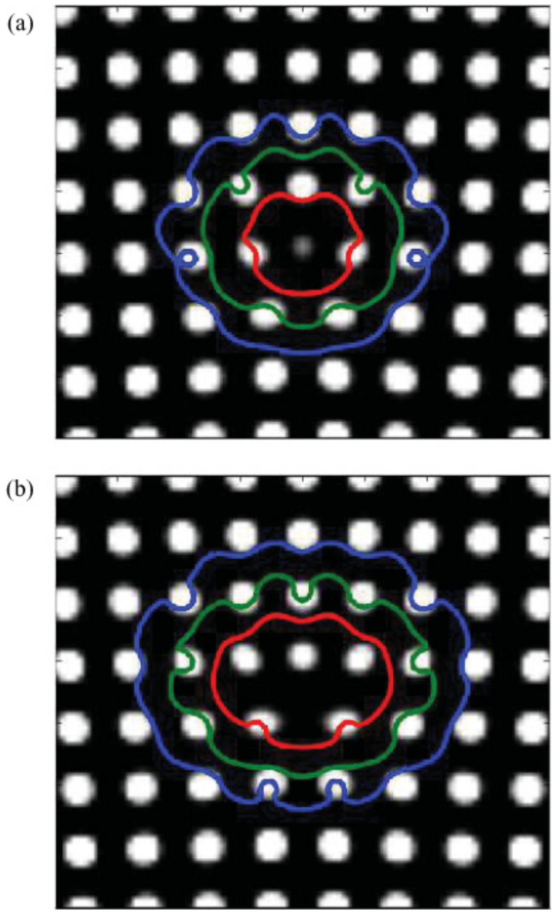

FIG. 6. (Color online) Solute segregation to an edge dislocation in 2D, forming part of a tilt boundary. The density profile is shown in gray scale. Contour plots show isocontours of $c = 0.12$, 0.13, and 0.14, from outside to inside, for (a) $\alpha_{1A} = 0.8\sqrt{2}$ and $\alpha_{2A} = 0.8$ for the square phase in element A (elastically isotropic case) and (b) $\alpha_{1A} = 0.8$ and $\alpha_{2A} = 0.8$ for the square phase in element A (elastically anisotropic case).

The second effect to note is the topology of the composition profile around the defect. In addition to increasing the value of the stiffness matrix element of the square phase, the elastic anisotropy can also be tuned by changing one peak width relative to the other. For an elastically isotropic matrix Fig. 6(a), the compositional profile around the defect is also relatively isotropic. There is still some anisotropy in the profile due to the anisotropic structure of the defect itself. However, as the stiffness matrix element becomes more anisotropic [Fig. 6(b)] the compositional profile around the defect also assumes a more anisotropic profile, featuring more elliptical isocontours of the composition field.

The third effect is in the density field itself. The triangular phase is essentially a sheared state of the square phase. Tuning the elastic coefficients such that the system can shear from the square state with no barrier into the triangular state is achieved by making the correlation peaks infinitely wide. By choosing a finite width for the correlation peaks, we are selecting the shear barrier which the system must overcome to transform from one state to the other. In the presence of a defect the system is in a state of frustration and attempts to form one state or the other. By decreasing the shear energy barrier the system will begin to choose a more triangular structure within the defect itself. This is shown in Fig. 6(a) through the emergence of a low-amplitude peak in the defect. In the case where the matrix element is stiffer and has a larger shear energy barrier, the density field that comprises the defect attempts to conform to the matrix topology, eliminating the emergence of the extra peak within the defect [Fig. 6(b)]. All of these effects play a role in the selection of the compositional and density profiles around the defects. The relaxed state of these fields will thus affect how defects move and interact with grain boundaries or other defects during thermomechanical processing.

V. SUMMARY

We have introduced a field crystal (PFC) methodology for structural transformations in binary alloys. We have shown how to construct the model in terms of a slowly varying composition field and an atomically modulated density field. In addition, we simplify the model for the case where the diffusion of impurities can be assumed to vary on length scales much longer than the interatomic distances. This simplified alloy model incorporates much of the structural information of the two separate elements by inclusion of the two different correlation functions, C_2^{AA} and C_2^{BB}. This allows each element's elastic properties to be entered into the model independently. The resultant behavior of the solid solution depends on the mixture of these correlation kernels. Even at this level of simplification we are able to simulate a robust range of realistic phase diagrams, including a peritectic phase diagram [Fig. 3(a)], eutectic phase diagrams (Figs. 4 and 5), and an isomorphous phase diagram [Fig. 3(b)].

The model itself opens up a plethora of potential applications where atomic scale elasto-plastic effects couple to the diffusive time scales governing many practical materials processes of interest in engineering alloys. We showcased two such examples in this paper. The first studied the lamellar spacing selection for both structurally similar and structurally dissimilar phases. Our binary PFC model makes it possible to study in a more natural way the elastic, orientational, and segregation effects of spacing and lamellar growth and coarsening. The second phenomenon examined is that of solute segregation to grain boundaries and defects in a material. The model incorporates both elastic and chemical interactions between the composition field and the density structure through the effective correlation function Eq. (11). Both of these effects were shown to cause segregation to defects and will play an important role in the migration of these defects and boundaries.

ACKNOWLEDGMENT

We thank the Natural Science and Engineering Research Council of Canada (NSERC) for financial support.

APPENDIX: AMPLITUDE MINIMIZATION AND FREE-ENERGY INTEGRATION

The construction of the energy curves is performed by making certain approximations to the density field which allow the mathematics to be more tractable. From Eq. (15) it can be seen that the fcc density approximation is constructed via two amplitudes. The free energy in Eq. (9) is integrated over a single unit cell using the following density approximation for each phase: constant, triangle, and square for 2D and constant, bcc, and fcc for 3D phase diagrams. The free-energy functional is reproduced here:

$$\frac{\Delta F}{kTV\rho_0} = \frac{1}{a^3}\int_{\mathrm{cell}} dV \left\{ \frac{n^2}{2} - \eta\frac{n^3}{6} + \chi\frac{n^4}{12} + \alpha|\vec{\nabla}c|^2 \right. \\ \left. + (n+1)\Delta F_{\mathrm{mix}}(c) - \frac{1}{2}n\int C_{\mathrm{eff}}^n(|r-r'|)n' \right\}, \tag{A1}$$

where V is volume over the unit cell.

Under the multimode approximation, the composition field is assumed to be constant in the bulk lattice and correspondingly, the gradient term in composition in this equation is zero. Likewise, the premultiplying component n to the $\Delta F_{\mathrm{mix}}(c)$ term integrates to zero over the unit cell, since the integration is completed around the reference density $\bar{n} = 0$. These considerations leave the following integral to be calculated:

$$\frac{\Delta F}{kTV\rho_0} = \frac{1}{a^3}\int_{\mathrm{cell}} dV \left\{ \frac{n^2}{2} - \eta\frac{n^3}{6} + \chi\frac{n^4}{12} \right. \\ \left. + \Delta F_{\mathrm{mix}}(c) - \frac{1}{2}n\int C_{\mathrm{eff}}^n(|r-r'|)n' \right\}. \tag{A2}$$

The $\Delta F_{\mathrm{mix}}(c)$ term is pulled from the integral entirely since it depends only on the smooth field c and is thus trivial to compute. The ideal component to the energy is also easy to integrate in terms of the density-mode approximation above, yielding a function in terms of the density amplitudes, A_1 and A_2, and the parameters η and χ. For example, inputting a two-mode general expression for a square density field yields $\Delta F_{id}/V = 2(A_1^2 + A_2^2) - 4\eta A_2 A_1^2 + 12\chi A_1^2 A_2^2 + 3\chi(A_1^4 + A_2^4)$. The trivial minimum of this energy is $A_1 = A_2 = 0$, in the limit of the ideal energy expansion. The particular choice of η and χ can lead to different minimizations of ΔF_{id} with nonzero amplitudes,[21] however, we restrict η and χ in ranges that have a zero amplitude minimization for the ideal energy.

The lattice spacing a nontrivially depends on composition, as it is linked to the form for the resultant correlation function based on bulk composition, C_{eff}^n. We consider two cases in this paper. The first is the case where the lattice spacings for the elements are similar. In this case the correlation peaks closely align and we treat the resultant peak positions to correspond to lattice spacings interpolated by the compositional interpolation functions, i.e., the lattice spacing for fcc in the peritectic phase diagram $a_{\mathrm{fcc}} = X_1 a_{\mathrm{fcc}}^A + X_2 a_{\mathrm{fcc}}^B$. The second is the case where the peaks in the correlation function do not align at all, as is the case for the square-triangle phase diagram of Fig. 5. Here we assume the lattice spacing does not vary greatly from the dominant structure, which can be seen by the very small shift in the peak positions in C_{eff}^n.

With this approximation, the convolution can be integrated mode by mode in the density expansion of Eq. (15). In Fourier space the convolution integral becomes trivial, with the periodic density expansion yielding a Dirac δ function so that the convolution returns the mode that was input, modulated by the correlation peak height at that mode frequency, i.e., $\int \hat{C}^n_{\text{eff}}(|r-r'|)n = \sum_m \int \hat{C}^n_{\text{eff}}(|r-r'|)n_m = \sum_m \hat{C}^n_{\text{eff}}(k=k_j)n_m$, where m denotes the individual modes in the density approximation. Summing over all the reciprocal space modes for a given density expansion and integrating over the unit cell gives an excess energy

$$\Delta F_{ex} = -M_1 A_1^2 \hat{C}^n_{\text{eff}}(k=k_1) - M_2 A_2^2 \hat{C}^n_{\text{eff}}(k=k_2), \qquad \text{(A3)}$$

where the different symmetries M_1 and M_2 take values of half of the number of modes used to construct the phase. A triangular phase, for instance, uses six modes in reciprocal space, corresponding to k_1 and zero modes for k_2, so that $M_1 = 3$ and $M_2 = 0$. Correspondingly, we use for square symmetry $M_1 = 2$ and $M_2 = 2$, bcc $M_1 = 24$ and $M_2 = 0$, and fcc $M_1 = 16$ and $M_2 = 12$. The function $\hat{C}^n_{\text{eff}}(k=k_j)$ is simply the value of the correlation kernel at the frequency of the mode in question. k_1 and k_2 are the resultant peak positions corresponding to the lattice position modified by the composition, i.e., $a_{\text{fcc}} = X_1 a^A_{\text{fcc}} + X_2 a^B_{\text{fcc}}$.

The total free energy per unit cell is therefore a fourth-order polynomial function in A_1 and A_2, and also a function of c and σ. Before constructing the phase diagram this polynomial must be minimized with respect to the amplitudes A_1 and A_2. To make this calculation tractable, we make a further assumption that the second amplitude of the two-mode density fields is a function of the first amplitude $A_2 = f A_1$. For the purpose of calculating the phase diagram we assume that f varies very little over the range of σ values we are interested in. We compute f explicitly for the case of $\sigma = 0$. For the square phase $f = 0.605$ and for the fcc phase $f = 0.568$. The amplitude is then easily minimized as a function of both c and σ, and is substituted back into the free energy, giving an energy as a function of c and σ only. These energies for the different structures are used to construct the phase diagrams.

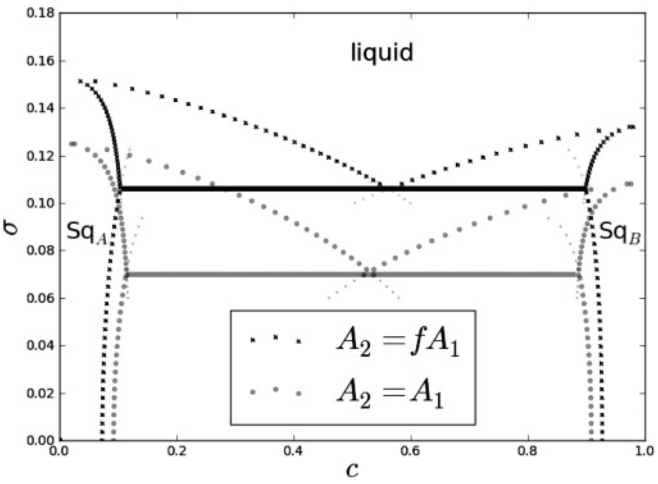

FIG. 7. Square-square phase diagrams showing both the two- and single-amplitude approximations. Parameters used for the calculation are given in the text.

Figure 7 shows a comparison between the phase diagram using our minimization technique that uses two amplitudes and which uses a single value for all amplitudes in the density expansion, i.e., where $A_2 = A_1$.[24] As mentioned previously, the qualitative features are not altered. However, the phase diagram undergoes a quantitative shift as a function of temperature.

---

[1] J. B. Collins and H. Levine, Phys. Rev. B **31**, 6119 (1985).
[2] J. Warren and W. J. Boettinger, Acta Metall. **43**, 689 (1995).
[3] A. Karma and W. J. Rappel, Phys. Rev. E **53**, 3017 (1996).
[4] N. Provatas, N. Goldenfeld, and J. Dantzig, Phys. Rev. Lett. **80**, 3308 (1998).
[5] N. Provatas, N. Goldenfeld, J. Dantzig, J. C. LaCombe, A. Lupulescu, M. B. Koss, M. E. Glicksman, and R. Almgren, Phys. Rev. Lett. **82**, 4496 (1999).
[6] B. Echebarria, R. Folch, A. Karma, and M. Plapp, Phys. Rev. E **70**, 061604 (2004).
[7] R. Folch and M. Plapp, Phys. Rev. E **72**, 011602 (2005).
[8] M. Greenwood, M. Haataja, and N. Provatas, Phys. Rev. Lett. **93**, 246101 (2004).
[9] I. Steinbach and M. Apel, Physica D-Nonlinear Phenom. **217**, 153 (2006).
[10] M. Haataja, J. Muller, A. D. Rutenberg, and M. Grant, Phys. Rev. B **65**, 035401 (2001).
[11] Y. U. Wang, Y. M. Jin, A. M. Cuitino, and A. G. Khachaturyan, Acta Mater. **49**, 1847 (2001).
[12] J. Zhu, T. Wang, A. Ardell, S. Zhou, Z. Liu, and L. Chen, Acta Mater. **52**, 2837 (2004).
[13] D. Yeon, P. Cha, J. Kim, M. Grant, and J. Yoon, Modell. Simul. Mater. Sci. Eng. **13**, 299 (2005).
[14] M. Greenwood, J. Hoyt, and N. Provatas, Acta Mater. **57**, 2613 (2009).
[15] K. R. Elder, M. Katakowski, M. Haataja, and M. Grant, Phys. Rev. Lett. **88**, 245701 (2002).
[16] K. R. Elder and M. Grant, Phys. Rev. E **70**, 051605 (2004).
[17] P. Stefanovic, M. Haataja, and N. Provatas, Phys. Rev. Lett. **96**, 225504 (2006).
[18] K. R. Elder, N. Provatas, J. Berry, P. Stefanovic, and M. Grant, Phys. Rev. B **75**, 064107 (2007).
[19] Y. M. Jin and A. G. Khachaturyan, J. Appl. Phys. **100**, 013519 (2006).
[20] M. Greenwood, N. Provatas, and J. Rottler, Phys. Rev. Lett. **105**, 045702 (2010).
[21] M. Greenwood, J. Rottler, and N. Provatas, Phys. Rev. E **83**, 031601 (2011).
[22] N. Provatas and S. Majaniemi, Phys. Rev. E **82**, 041601 (2010).
[23] S. Majaniemi and N. Provatas, Phys. Rev. E **79**, 011607 (2009).
[24] K. R. Elder, Z. F. Huang, and N. Provatas, Phys. Rev. E **81**, 011602 (2010).
[25] Z. F. Huang, K. R. Elder, and N. Provatas, Phys. Rev. E **82**, 021605 (2010).